

Understanding the Formation Mechanisms of Silicon Particles from the Thermal Disproportionation of Hydrogen Silsesquioxane

Published as part of the *Chemistry of Materials virtual special issue* “in Honor of Prof. Clement Sanchez”.

Cynthia Cibaka-Ndaya,* Kevin O'Connor, Emmanuel Opeyemi Idowu, Megan A. Parker, Eric Lebraud, Sabrina Lacomme, David Montero, Paula Sanz Camacho, Jonathan G.-C. Veinot, Ioan-Lucian Roiban,* and Glenna L. Drisko*



Cite This: *Chem. Mater.* 2023, 35, 8551–8560



Read Online

ACCESS |



Metrics & More

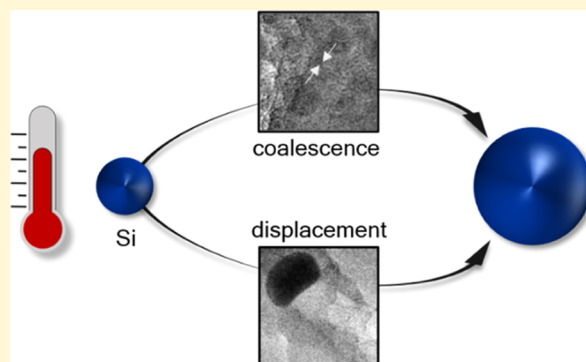


Article Recommendations



Supporting Information

ABSTRACT: Crystalline silicon particles sustaining Mie resonances are readily obtained from the thermal processing of hydrogen silsesquioxane (HSQ). Here, the mechanisms involved in silicon particle formation and growth from HSQ are investigated through real-time *in situ* analysis using an environmental transmission electron microscope and X-ray diffractometer. The nucleation of Si nanodomains is observed starting around 1000 °C. For the first time, a highly mobile intermediate phase is experimentally observed, thus demonstrating a previously unknown growth mechanism. At least two growth processes occur simultaneously: the coalescence of small particles into larger particles and growth mode by particle displacement through the matrix toward the HSQ grain surface. Postsynthetic characterization by scanning electron microscopy further supports the latter growth mechanism. The gaseous environment employed during synthesis impacts particle formation and growth under both *in situ* and *ex situ* conditions, impacting the particle yield and structural homogeneity. Understanding the formation mechanisms of particles provides promising pathways for reducing the energy cost of this synthetic route.



INTRODUCTION

In the development of optical metamaterials with high scattering efficiency, silicon (Si) particles are excellent candidates for meta-atoms, although they should fulfill particular requirements regarding their size, crystallinity, and density to support Mie resonances.^{1,2} Specifically, for optical applications in the visible region, particles should be between 75 and 200 nm, highly crystalline, and nonporous. Applications of resonant Si particles include anticounterfeit labels,³ nonlinear nanophotonics,⁴ and enhanced Raman scattering,^{5,6} among others. Optimizing a bottom-up synthesis method to easily obtain resonant units with the desired characteristics could open pathways toward large-scale fabrication of highly efficient metamaterials.^{7,8} One of the most promising fabrication methods currently available is the thermal disproportionation of silicon-rich oxide compounds, in particular hydrogen silsesquioxane (HSQ), $[\text{HSiO}_{3/2}]_n$ producing objects that fully possess the desired criteria for resonant silicon particles.^{9–13} The main drawbacks of this synthesis are that the synthesis occurs at very high temperatures, and thus is energy-intensive, and that the particles produced are polydisperse in size, and thus need to undergo a size separation process in order to obtain a monodisperse

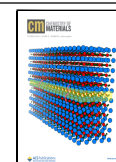
sample.^{12,14,15} Perhaps by understanding the particle formation mechanism, it would be possible either to decrease the polydispersity or to decrease the energy requirements of this synthetic approach.

Despite a few decades of research in this domain, the formation mechanism of the silicon particles via HSQ disproportionation is still not fully understood, particularly above the Si melting point. Several studies report a decrease in the number of silicon nanocrystals, coupled to an increase in their size with increased annealing temperature, which has been hypothesized to be due to Ostwald ripening.^{14,16–19} The dissolution of small crystalline particles to the benefit of larger ones in the solid state is curious. These studies mostly involved postsynthetic analysis using various techniques, for example, the use of different modes in electron microscopy coupled with atomic simulations.^{17,20} However, particle coalescence would

Received: June 11, 2023

Revised: September 2, 2023

Published: October 11, 2023



also lead to the same postsynthetic observations. In fact, a theoretical study using a combination of quantum mechanical and Monte Carlo simulations suggested two different growth regimes driven by oxygen atom diffusion in a silicon-rich oxide compound.²¹ The first one, which the authors claim to occur more frequently, is a coalescence-like phenomenon. Two particles in close proximity are not attracted to each other but combine into a single particle due to the out-diffusion of oxygen in the interspace between them. The second growth regime is a pseudoripening process in which the small particles do not dissolve but instead reoxidize, thus transferring Si species back into the silicon oxide matrix, which will then be available for the growth of larger particles. Experimental observations of the high-temperature process are needed to validate these simulations.

The present work aims to unveil the mechanism of particle formation by investigating the nucleation and growth processes of Si particles from the thermal disproportionation of HSQ, while examining the role of the inert versus reducing atmosphere in particle formation. The clear establishment of the phenomena occurring during the transformation of the initial matter requires advanced characterization techniques such as *in situ* analyses that probe the changes from the initial precursors toward the resulting particles in real time. Particularly, environmental transmission electron microscopy (ETEM) allows direct observation of matter transformations, as it interacts with the environmental medium (gas or liquid phase, heating, or cooling conditions). The use of this technique offers a new perspective, as previous studies mostly proceeded by postsynthetic analysis of *ex situ* prepared materials.^{16,22}

Here, the formation of Si particles from HSQ was investigated using ETEM. For the first time, a highly malleable and mobile phase, inducing significant particle growth, has been observed experimentally. Multiple growth processes were found, including particle–particle coalescence and more surprisingly a displacement of the particles through the matrix leaving traces in their wake due to interfacial chemical reactions. The real-time observations were complemented with postsynthetic SEM analysis of large particle samples, supporting the growth mechanisms identified in ETEM. *In situ* XRD measurements up to 1200 °C demonstrated a growth mode at the solid state below the melting point of Si. In addition, an investigation by ²⁹Si MAS NMR spectroscopy revealed that thermally processing HSQ under a reducing atmosphere (H₂) induces more segregation of Si domains; however, they are less homogeneous than when formed under inert conditions (Ar).

RESULTS AND DISCUSSION

In the bottom-up preparation of Si particles from HSQ, spherical silicon particles result from the thermal decomposition of HSQ at high temperatures (>1000 °C), which leads to disproportionation into crystalline Si particles embedded in a matrix of silica.^{9–11} The size of the resulting silicon particles can be tailored by adjusting the processing temperature.^{10,11} In a typical synthesis, the particles are then collected after etching the silica matrix with hydrofluoric acid (HF). In the present work, the last step is not used. Instead, the evolution from HSQ at room temperature to oxide-embedded Si particles at 1300 °C is studied in depth to explore silicon nucleation and growth processes.

Nucleation of Si particles. The decomposition of HSQ first generates matrix-embedded nuclei, as observed by ETEM in a selected area (Figure 1). Figure 1b displays early stage

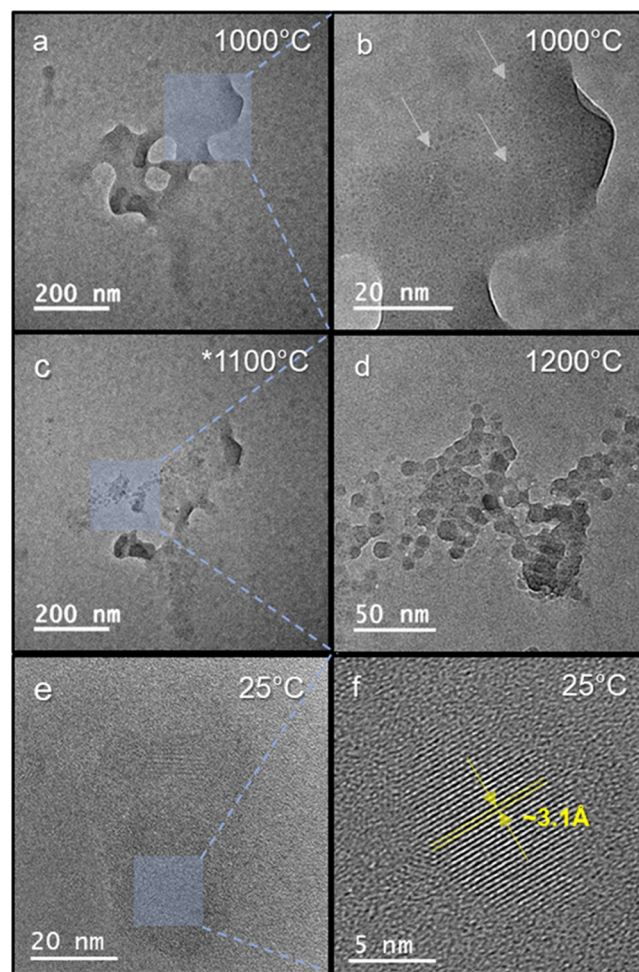


Figure 1. Particle nucleation upon thermal processing of HSQ in a gaseous atmosphere (~ 20 mbar) of argon. (a) Area probed at the early stage of nucleation. (b) Higher magnification of a selected region in this area. The higher magnification allows nuclei of about 1 nm to be observed (some are designated by gray arrows). (c, d) With a temperature increase to 1200 °C, the nuclei evolve to small particles of about 7 nm. (*) The image in (c) shows the probed area upon cooling to 1100 °C, after growth of particles at 1200 °C for a better comparison. (e, f) Images collected in the probed area at room temperature after annealing show the obtained crystalline domains with *d*-spacing consistent with diamond cubic Si(111) planes.

particle formation at 1000 °C, with the presence of very small nuclei of about 1 nm visible in the image. The subsequent heating of the analyzed sample resulted in the growth of nuclei. At 1200 °C, particles of 7 nm diameter were obtained as seen in Figure 1c,d. Under high temperature and set magnifications, it was difficult to assess the crystallinity of the formed particles. Further high-resolution analyses of this region, upon cooling to room temperature, revealed the presence of crystalline Si domains as shown in Figures 1e,f and S1, with a *d*-spacing value consistent with cubic diamond Si(111) planes. In addition, Figure S1b shows that more nanodomains of crystalline silicon were found in different regions of the sample. These areas were subjected to the same thermal treatment but were not illuminated by the electron beam

during the process. These observations confirm that up to this temperature, particle nucleation and growth essentially originate from the thermal processing of the sample.

These observations are consistent with those reported in previous papers.^{16,22,23} These studies conclude that the thermal treatment of silicon-rich oxide compounds induces first the segregation and growth of amorphous Si clusters in the approximate temperature range of $\sim 400\text{--}800\text{ }^{\circ}\text{C}$. The amorphous Si domains then crystallize around $900\text{ }^{\circ}\text{C}$ and grow. Both the nucleation and the phase transition temperatures from amorphous to crystalline were dependent on the initial composition of the sample of silicon-rich oxide. In the present study, the ETEM conditions (pressure around 20 mbar and set magnification) did not allow observation of subnanometer silicon domains, if these formed below $1000\text{ }^{\circ}\text{C}$. Particle nucleation was inhomogeneous throughout the sample. Some regions did not present nuclei, even at the peak temperature of $1300\text{ }^{\circ}\text{C}$ (Figure S2). This is likely due to differences in the local composition of the initial HSQ sample. HSQ was made by a wet-chemistry route (partial hydrolysis and polymerization), so it is possible that the local stoichiometry in any given area of the HSQ could vary, even within the same sample. In addition, HSQ is composed of cage and ladder structures and local variations of the cage: ladder ratio might also impact the resulting nanoparticles.²⁴ The influence of HSQ inhomogeneity on particle synthesis remains an active area of study. Other areas of the sample showed an abundance of nuclei, which progressively grew in size with increasing temperature.

Particle Growth. At temperatures of 1200 and $1300\text{ }^{\circ}\text{C}$, the silicon underwent a phase transition to a malleable state with high mobility. At this stage, two different mechanisms were identified for particle growth: the coalescence of particles and the growth during displacement through the matrix.

A video provided in the Supporting Information (Video S1) shows the observed coalescence of particles. Figure 2 presents

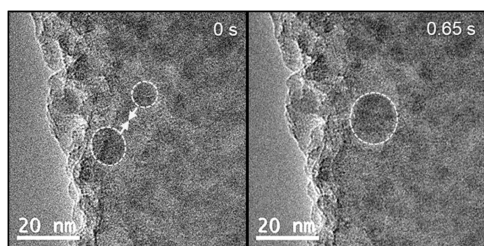


Figure 2. Growth was achieved via particle coalescence. Images are collected at the set temperature of $1200\text{ }^{\circ}\text{C}$ in a gaseous atmosphere (~ 20 mbar) of 95% N_2 and 5% H_2 . (a) At $t = 0$ s, two particles are well separated. They both displace toward the other particle and coalesce into a single particle.

the images retrieved from this video before and after coalescence occurs. The video shows a decelerated coalescence for better visualization; however, the actual video timespan is about 1.2 s and the observed phenomenon occurred in less than one second. The two particles, with respective apparent diameters around 8 and 11 nm, displaced simultaneously toward each other, indicating a high mobility of the particles. The combined larger nanoparticle presented a diameter of about 14 nm, albeit nonspherical in shape.

A second growth mechanism has been observed via particle displacement in the matrix, shown in Video S2 in the

Supporting Information. From this video, three representative images are shown (Figure 3) of a particle moving and changing shape during 14 s timespan. Here, the morphological changes of the particle throughout the recorded period demonstrate a highly malleable phase: the sphere-like shape evolves into less defined conformations in the manner of a liquid droplet filling a constrained volume or due to capillary action on a rough surface. A trace is left in the wake of the nanoparticle as it moves through the matrix. This suggests that interfacial chemical reactions occur between the particle surface and silicon oxide, resulting in the addition of reduced Si from the matrix to the particle. Although the changes are much less pronounced, the same phenomenon takes place in the case of a second particle present in the probed area at the bottom of the images in Figure 3.

Video S3 and associated Figure 4 clearly summarize the identified growth mechanisms. Black arrows, serving as a guide to the eye in Figure 4a, indicate the coalescence of two particles with the resulting larger particle seen in Figure 4b. This particle starts to move across the matrix, as tracked with the green arrows in Figure 4b–f. Figure 4d shows the particle with a morphological change consistent with malleable behavior. In addition, in Figure 4d–f, a trace formed upon displacement of the particle within the matrix is observed. The probed area displays a second coalescence event, shown by the black arrows in Figure 4c–e. Only a limited number of coalescence events were witnessed in these experiments; however, it is reasonable to suppose that this growth mechanism occurs regularly between closely spaced particles with high malleability and mobility. The particles minimize their surface energy upon coalescing into a single particle. One possible explanation of this phenomenon could be the out-diffusion of oxygen in the interspace between closely spaced particles, as suggested by previously reported Monte Carlo simulations.²¹ This previous study mentioned that coalescence-like occurrences largely contribute to the growth mechanism, which has been experimentally validated in the present work. Moreover, it can be observed that toward the center of the matrix grain imaged here, there is a large particle, which is hardly visible in the center of Figure 4a, which becomes progressively more defined by Figure 4f. It appears as though this particle is moving through the matrix, with a displacement in the direction parallel to the electron beam.

The particles seem to move toward the surface of the matrix grains in which they are embedded. During the *in situ* experiments, the particles disappeared very quickly under the electron beam upon reaching the surface and losing the protection of the matrix. Because of this, it was difficult to investigate in real time how the particles behave upon cooling.

Figure S3 shows that differences are found in the particles obtained by standard *ex situ* annealing and *in situ* heating in the ETEM at $1300\text{ }^{\circ}\text{C}$. An obvious size discrepancy is observed, with an average diameter of 12 nm for *ex situ* prepared particles, whereas the particles have sizes between ~ 30 and ~ 100 nm in *in situ* experiments. In addition, ETEM experiments were carried out in either 100% argon or a mixture of 95% nitrogen and 5% hydrogen, and Si particles demonstrated a high mobility and substantial growth only when the chamber was filled with a mixture of N_2 and H_2 . The formation of small particles at $1000\text{ }^{\circ}\text{C}$ was achieved independently of the gas used. The most probable explanation for the observed large particles in ETEM experiments is fast growth induced by the highly reducing character of the

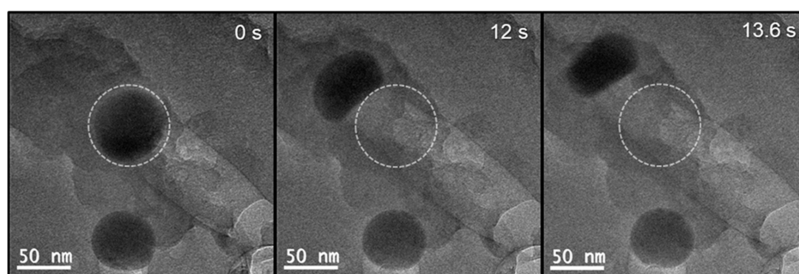


Figure 3. Growth via displacement in the matrix. Images are collected at the set temperature of 1300 °C in a gaseous atmosphere (~ 20 mbar) of 95% N_2 and 5% H_2 . The particle displaces from its initial starting point (indicated by a gray dashed circle) over the course of 14 s of observation.

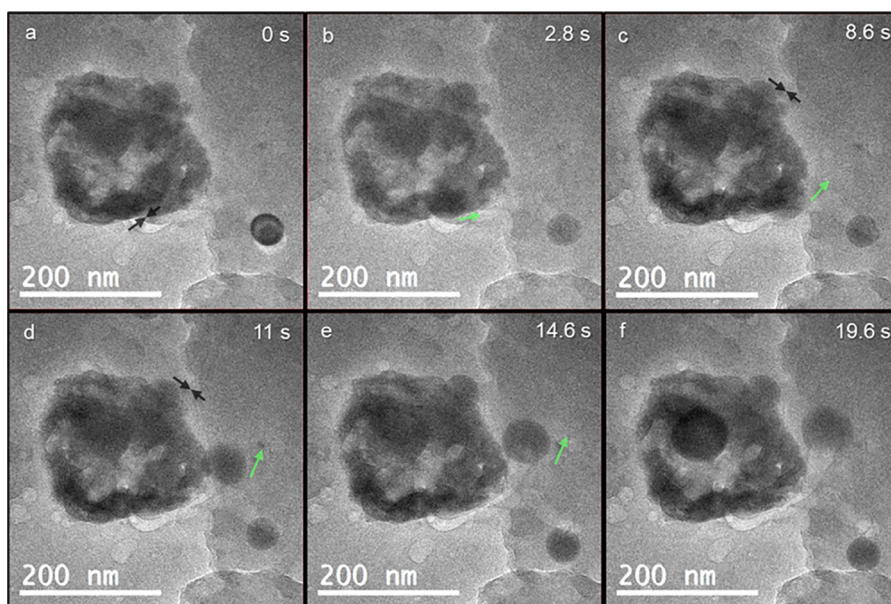


Figure 4. Images summarizing the observed growth modes with particles showing a highly malleable phase. Growth via coalescence and displacement inside the matrix are observed with time, with the video showing that (a) 0 s, (b) 2.8 s, (c) 8.6 s, (d) 11 s, (e) 14.6 s, and (f) 19.6 s have elapsed since the beginning of the filming. Images are collected at the set temperature of 1300 °C in a gaseous atmosphere (~ 20 mbar) of 95% N_2 and 5% H_2 .

electron beam coupled with the presence of H_2 at 1300 °C in the microscope chamber. However, it is difficult to quantify precisely the extent of the electron beam effect. Several aspects should be taken into account, including the total electron dose sent to the probed area. The synergistic effects enhancing reducing conditions will be the subject of further investigations. Regarding the observed mobility of the growing particles, several aspects might be considered at the temperature of experiments, including the Tamman effect, which induces atomic mobility at a much lower temperature than the melting point. There is melting point depression for nanoscale objects, which might also influence the experiments.

Nonetheless, the growth modes observed for large particles in ETEM seem to be consistent with the growth mechanisms of larger particles under *ex situ* thermal treatment above the melting point of Si (~ 1410 °C for bulk Si).¹⁴ To support this, postsynthetic analysis of samples was carried out through *ex situ* heating at temperatures higher than the melting point of Si, i.e., 1700 and 1500 °C. Figure 5 shows images collected from SEM analysis of these samples, supporting the growth mode by the displacement of highly mobile particles toward the surface. Figure 5a,b shows the surface of an untreated grain after thermal processing. Particles are observed emerging from the grain surface, which is more easily seen in the magnified image

in Figure 5b. This particle partially emerged from the matrix, with part of the silicon still embedded. Note that Figure 5b reveals a pseudospherical shape: facets, formed upon crystallization of the particle when the temperature decreases, are visible on a roughly spherical particle. An additional example of a particle is provided in Figure S4 to better visualize these facets. These features are typically not observed after HF etching in the standard fabrication of Si particles via disproportionation of silicon-rich oxide compounds. Figure 5c,d presents the internal regions of broken HSQ grains from the *ex situ* heated samples. The images are characterized by holes left after the displacement of particles as well as bumps from particles in the process of moving through the matrix. Traces are visible, where it seems that these tracks are globally oriented in the same direction. This observation suggests that particle displacement may be driven by differences in the density of the silicon particles relative to the matrix (Archimedes' principle). The collected information from SEM analysis supports that the growth mechanisms observed in the ETEM are consistent with what occurs in standard preparations of large Si particles.

Elemental analysis (STEM-EDX) was performed on the sample *ex situ* heated at 1700 °C in order to confirm the elemental composition of the formed crystalline particles. The

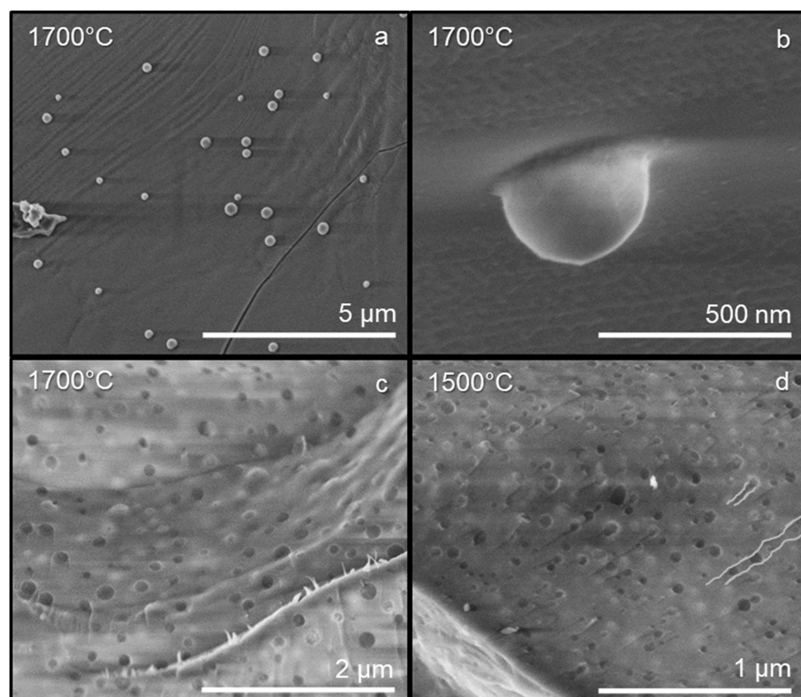


Figure 5. SEM analysis of samples *ex situ* heated to 1700 and 1500 °C under 1 bar of Ar. (a) Particles emerging from the surface of a grain; Temp. = 1700 °C. (b) Higher magnification of a selected particle with a view angle that highlights the particle emerging from the matrix; Temp. = 1700 °C. The inner region of a broken grain: holes, traces, and bumps are observed in (c) Temp. = 1700 °C and (d) Temp. = 1500 °C.

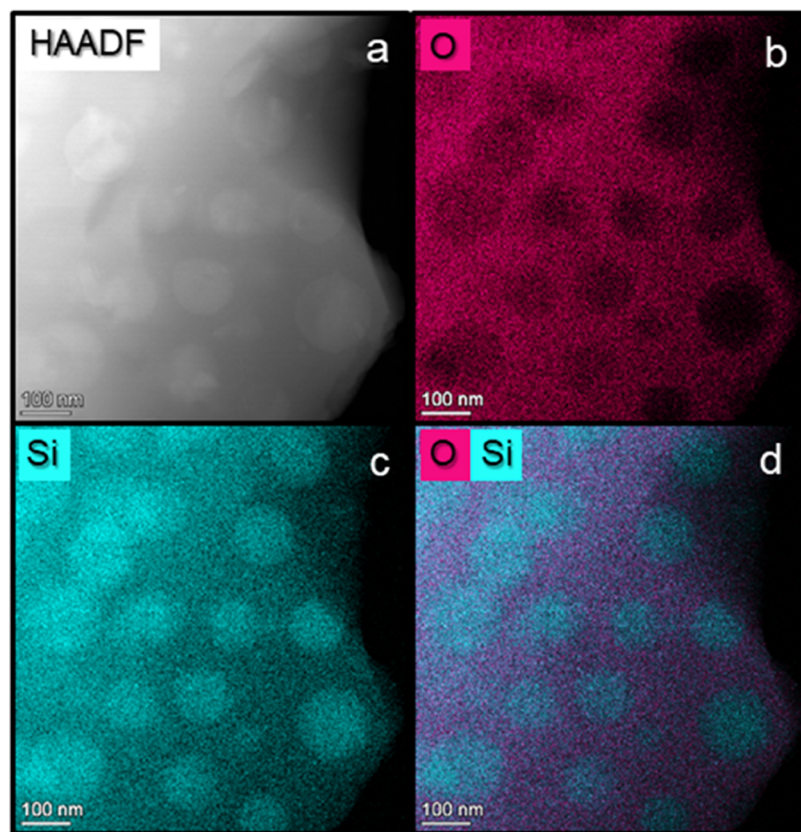


Figure 6. Post-synthetic STEM-EDX mapping in high vacuum of a sample *ex situ* heated to 1700 °C under Ar. (a) High-angle annular dark-field imaging of the probed region. (b) Oxygen mapping. (c) Silicon mapping. (d) Overlapping mapping of oxygen (in magenta) and silicon (in blue).

results of this analysis are presented in Figure 6a–d. The dark-field image in Figure 6a shows the presence of particles, with a brighter contrast, within the matrix. A deficit of oxygen is

identified at the location of the formed particles (Figure 6b), where there is a surplus silicon in these regions (Figure 6c). The overlapping of oxygen and silicon elemental mapping

unambiguously shows that the silicon particles are surrounded by a silicon oxide matrix (Figure 6d).

To further explore the real-time mechanism without the influence of the electron beam, complementary *in situ* XRD measurements (Figure 7) validate that below the melting point

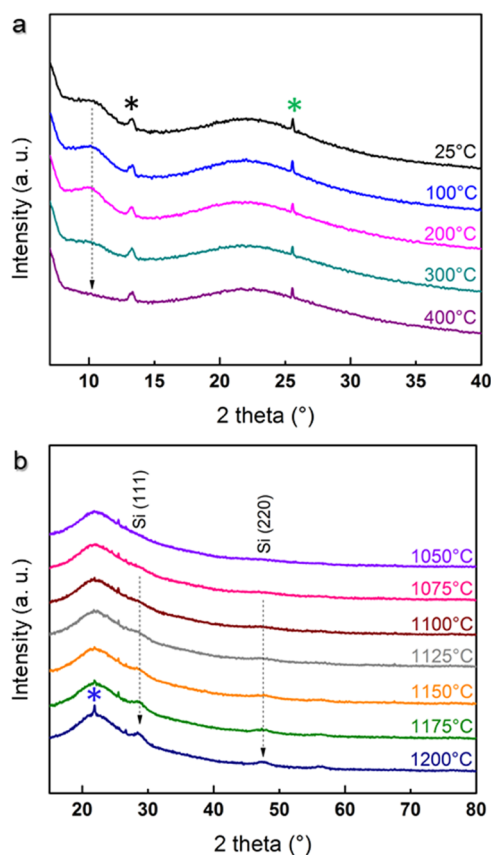


Figure 7. *In situ* powder XRD analysis of HSQ thermal treatment. (a) Diffractograms recorded from room temperature to 400 °C highlighting the feature around 10° 2 θ . The starred peak at 26° 2 θ is associated with the alumina sample holder. Black stars at 13° 2 θ designate an additional unexpected peak. (b) Diffractograms recorded from 1050 to 1200 °C highlight the progressive appearance of the cubic diamond Si signal. The dark blue star at 22° 2 θ designate an additional unexpected peak.

of Si, a growth route in the solid state takes place. XRD diffractograms were recorded upon thermal annealing of HSQ from room temperature to 1200 °C under nitrogen. The diffractograms displayed in Figures 7b and S5 reveal that approaching 1100 °C, the size of the Si crystallites becomes large enough to induce a diffraction signature. When the temperature is progressively raised to 1200 °C, the intensity of the peaks increases, indicating a greater ratio of crystallites to amorphous content, consistent with the crystallization of the nuclei. The sharpness of the peaks increases very slightly, indicating limited particle growth. The crystallinity is conserved during the dwell time of 1 h at 1200 °C as well as upon sample cooling (Figure S5). Thus, below the melting point of Si, crystallization is progressive with slow growth. Note that independent of the temperature, an amorphous phase dominated the XRD patterns due to the presence of the SiO_x matrix surrounding the Si nanocrystals. Moreover, below 400 °C, diffractograms in Figure 7a reveal a broad signal around 10° 2 θ , which progressively disappears upon increasing

the temperature up to 400 °C. This feature may relate to the subtle changes in the Fourier transform infrared spectra, reported by Hessel et al. for *ex situ* processed HSQ below 400 °C.²² While definitive assignments of these structural changes are yet to be made, the authors suggested HSQ crosslinking and cage rearrangement to be at the origin of the modifications in the initial HSQ FTIR spectrum. The peak at 13° 2 θ , present initially, could not be assigned; however, it did not show any modifications during the experiment. A peak at 22° 2 θ , distinguished at 1200 °C, might be associated with a small fraction of tetragonal SiO₂.

Influence of a Reducing Atmosphere. In the literature, the preparation of Si particles from the thermal processing of silicon-rich oxide compounds is conducted either in a reducing (presence of H₂) or an inert atmosphere. In the present work, the potential influence of hydrogen in this synthesis route was examined. For this purpose, samples were *ex situ* annealed at three different temperatures (1100, 1200, and 1300 °C) in the presence (95% Ar–5% H₂) and absence (100% Ar) of hydrogen. Samples were weighed before and after thermal annealing. The weight loss found for all of the samples (Table S1) did not present large variation and remained around 5% with only a very slight increase found under the reductive atmosphere compared to inert conditions. The weight loss of 5% is consistent with previously reported thermogravimetric analysis under a 95% N₂–5% H₂ mixture⁹ and under pure argon.²⁵ In this later work, the 5% weight loss was attributed to the release of SiH₄ and H₂ species using TGA coupled with mass spectrometry. Here, the obtained oxide-embedded particles were characterized using ²⁹Si MAS NMR spectroscopy, Raman spectroscopy, X-ray diffraction spectroscopy, and TEM. Micrographs of the prepared samples are presented in the Supporting Information (Figure S6) and confirm the formation of oxide-embedded nanoparticles. Figure 8 shows the spectroscopic analyses of the samples treated at 1300 °C.

The direct excitation ²⁹Si MAS NMR spectra show different local Si environments for the materials synthesized in a mixed atmosphere of Ar/H₂ compared to that of pure Ar. Both materials exhibit two well-separated signals coming from the silica matrix (highlighted in orange) and the silicon formed domains (highlighted in green). Provided as a guide, deconvolutions of the spectra are given in Figure S7 in the Supporting Information. A signal at around –110 ppm is present in both cases, associated with Q₄ species in the SiO₂ matrix. The material synthesized in a pure Ar atmosphere exhibits a very sharp peak (fwhm = 4 ppm) at –81 ppm, previously attributed to c-Si in a highly ordered environment.^{26–29} A larger signal around –66 ppm (fwhm = 20 ppm) is also found. This latter feature is also observed in the material synthesized in the presence of hydrogen: a very large Gaussian-like resonance centered at –67 ppm and spanning over –100 ppm. The signal centered at –67 ppm is between the expected responses of elemental silicon in amorphous and crystalline phases (around –40 ppm and –80 ppm, respectively).^{29,30} Perhaps this resonance originates from a distribution of chemical shifts as a consequence of local structural disorder or unidentified molecular species. Structural disorder due to strain, structural defects, or a large fraction of near-surface sites was previously reported to induce a large range of chemical shifts as well as a broadening of the responses from amorphous or crystalline silicon.³¹ Under reductive synthesis conditions, despite being not well separated, a contribution of c-Si in a highly ordered environment around –81 ppm cannot be

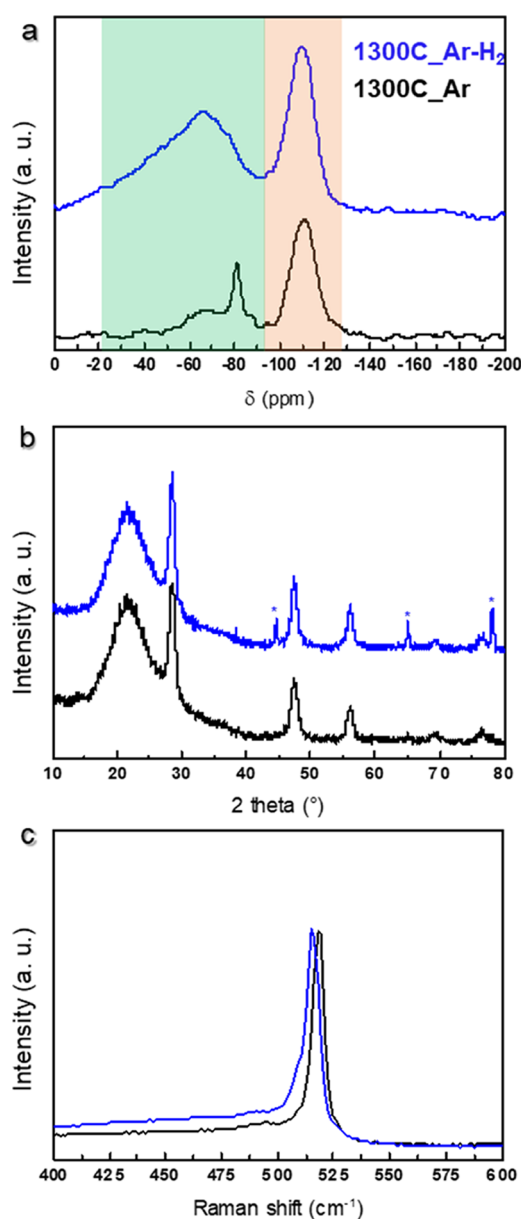


Figure 8. Influence of the presence of H₂ during particle synthesis. Spectroscopic analyses of samples *ex situ* annealed at 1300 °C under 100% Ar (black) and 95% Ar–5% H₂ (blue). The spectra are not normalized, and the y-axis provides the intensity in arbitrary units. (a) Direct excitation ²⁹Si MAS NMR spectra. The spectra are vertically translated for better comparison. (b) Powder X-ray diffraction patterns. Stars designate peaks from the aluminum powder XRD holder. (c) Representative Raman spectra.

excluded as this peak spans over -100 ppm. In addition, a signal around -37 ppm is found in the deconvolution of the response of the sample prepared under a reducing atmosphere. This feature could be associated either with amorphous silicon or with H₂Si(-SiH₃)-OSiH₃ species.³² Overall, it seems that the presence of hydrogen favors the segregation of Si species (higher percentage associated with the elemental Si signal; see Table S2), but the silicon within the nanoparticles is in a more complex environment. In contrast, under inert conditions, the retrieved percentages of silica were higher and the signal from Si domains suggested a more homogeneous environment. This result supports different chemical reduction pathways when

thermally processing HSQ under inert and reducing atmospheres. The same observations were made for the samples prepared at 1200 and 1100 °C. In addition, and as expected, the formation of Si domains was favored by higher temperatures (see Figure S7). Moreover, slight shifts to higher resonance frequency of the peak centered at -67 ppm are observed for the materials synthesized in a mixed atmosphere at 1200 and 1100 °C. This might be related to a decrease in particle size from around 12 nm to less than 6 nm (from TEM), as previously observed by Thiessen et al.³³ This is, however, less evident for the material synthesized in a pure Ar atmosphere.

Representative patterns obtained from XRD measurements and Raman spectroscopy analysis of samples prepared at 1300 °C are given in Figure 8b,c. In the presence and absence of H₂, the XRD patterns overlap well, although the fwhm in the case of the reducing conditions is slightly narrower (fwhm (2θ) of 0.74° compared to 0.82° in pure Ar), suggesting a slightly bigger crystallite size on average (11.6 nm compared to 10.5 nm in pure Ar from Scherrer calculations).

Raman spectroscopy is known to be a very sensitive probe for the local atomic bond order and particle size. The distinct Raman responses are known to be around 520 cm^{-1} for crystalline and 480 cm^{-1} for amorphous bulk silicon.^{34–38} In Figure 8c, both samples exhibit Raman responses near the signal expected for crystalline silicon. A very slight red shift ($\sim 3\text{ cm}^{-1}$) is observed for the sample under reducing conditions, but both values remain in the previously reported range for crystalline Si.³⁵ Red shifts ($>7\text{ cm}^{-1}$) have previously been attributed to incomplete or incipient crystallization as well as various sizes of crystallite in the sample³⁹ and intermediate range order.^{36,40} The work of Anastassakis et al. mentioned stresses in the sample at the origin of slight shifts.⁴¹ For small particles, the average bond energy within a particle decreases and thus so does the Raman frequency. In the present study, taking into account that the obtained shift at 1300 °C is very small and was not observed at 1200 °C (Figure S8) and that the XRD patterns seem to favor a slightly higher crystallinity in the case of hydrogen in the medium, it is likely that the crystallinity of both samples does not differ considerably. Possible differences in the structural defect density, as observed by NMR spectroscopy, may explain the differences in bond order.

CONCLUSIONS

This study elucidated two mechanisms taking part in the fabrication of Si particles from thermal annealing of HSQ, which may occur in place of or in addition to the Ostwald ripening process that has been proposed by others in the field. In particular, the ETEM analysis distinguished different growth pathways. For the first time, a highly malleable and mobile silicon phase was observed in real time, which led to substantial particle growth, reaching sizes typically obtained only above the melting point of Si. Growth processes by particle coalescence and particle displacement in the matrix toward the surface were identified. SEM analysis of *ex situ* prepared samples of large particles further supported the growth mechanisms identified by *in situ* observations. Most likely, fast particle growth resulted from the coupling between the reducing character of the electron beam, the presence of H₂ and heat. Therefore, it seems that one way to optimize this synthesis route to reduce energy consumption, while obtaining

silicon particle sizes large enough to support Mie resonance, is to provide a highly reducing environment during the reaction.

In addition to the ETEM investigations, *in situ* XRD measurements indicate that crystalline Si domains grew slowly in the solid state below the melting point. This study was complemented by an investigation of the role of a reducing atmosphere in the disproportionation reaction. ^{29}Si MAS NMR spectroscopy results underlined that different chemical pathways might occur in the presence or absence of hydrogen. A reducing atmosphere seems to induce the formation of more Si domains; however, they are less homogeneous.

EXPERIMENTAL SECTION

Materials. Toluene (HPLC grade), fuming sulfuric acid (reagent grade, 20% free SO_3 bases), and trichlorosilane (99%) were purchased from MilliporeSigma. Sulfuric acid (reagent grade, 95–98%) was purchased from Fisher Scientific. Dry toluene was dispensed from a Pure-Solv purification system with N_2 operating gas; other reagents were used as received.

Preparation of Hydrogen Silsesquioxane. HSQ was synthesized using an adapted literature procedure.³³ On an Ar-charged Schlenk line, concentrated sulfuric acid (15 mL) and fuming sulfuric acid (7 mL) are mixed in a purged, 2 L, 3-neck round-bottom flask. Dry toluene (45 mL) is added dropwise with stirring, followed by a dropwise addition of trichlorosilane (16 mL) in dry toluene (110 mL) overnight. Both additions occur under flowing Ar. The mixture is then decanted into a separatory funnel, isolating the organic layer, and washed three times with a solution of aqueous sulfuric acid (1.2 L of H_2O , 0.4 L H_2SO_4). The washed organic layer is dried and neutralized over MgSO_4 and CaCO_3 overnight. Following gravity filtration, toluene is removed via rotary evaporation followed by a final evaporation under vacuum, yielding a white solid.

In Situ Investigations. ETEM Experiments. *In situ* TEM experiments were performed using an FEI ETEM Titan 80-300 microscope operating at 300 kV equipped with a OneView camera from Gatan. The as-received HSQ grains were ground and dispersed in 2-propanol. Drops of the highly dilute dispersion were deposited on a Si_3N_4 window chip purchased from DENS solutions, compatible with the Wildfire sample holder. The solvent was evaporated under air prior to analysis. During experiments, the microscope chamber was filled with a flow of gas at a pressure of around 20 mbar. Experiments were performed under pure argon or under a mixture of N_2 – H_2 (95–5%). In a typical experiment, the temperature was raised from room temperature to 800 °C at a rate of 10 °C/s with ~2 min of plateau every 100 °C. TEM images were not systematically collected in this temperature range. From 850 to 1300 °C, the temperature was increased by a step of 50 °C, at a rate of 10 °C/s with plateaus of about 20 min – 1 h at 900, 1000, 1100, 1200, and 1300 °C in order to collect images and record videos. Note that the chips used are certified for sustaining temperatures up to 1100 °C; however, a progressive slight increase of the temperature allowed 1300 °C to be reached without damaging the chip. Cooling the sample to room temperature was carried out with step sizes of 100 °C at a rate of –10 °C/s.

In Situ XRD. *In situ* X-ray diffractograms in the range of 4–100° 2θ were collected using a PANalytical X'Pert Pro apparatus (*Co radiation) equipped with an Anton Paar HTK1200 high-temperature chamber. XRD measurements were carried out under a flow of nitrogen upon heating and cooling in the range of 25–1200 °C. The temperature profile was set as follows: from 25 to 100 °C, the temperature was increased at a rate of 60 °C/min. From 100 to 900 °C, a rate of 2 °C/min was applied, and sample XRD responses were collected every 100 °C corresponding to 30 min dwell time. From 900 to 1200 °C, diffractograms were collected every 25 °C. A dwell time of 1 h was set at 1200 °C before cooling the sample at a rate of –2 °C/min with signals collected every 25 °C until reaching 1000 °C and then every 100 °C until 100 °C. From 100 to 25 °C, a decrease rate of 5 °C/min was used.

(* Cobalt radiation was used during *in situ* XRD measurements, and the collected diffractograms were afterward converted to signals from Co to Cu ($K\alpha$) wavelength using software PowDLL Converter.

Ex Situ Investigations. Sample Preparation. *Ex situ* annealing of HSQ samples was performed in an oven under a constant gas flow rate at atmospheric pressure. HSQ powder was disposed in a crucible and introduced in the oven. For target temperatures of 1100, 1200, and 1300 °C, alumina crucibles were employed. The temperature was raised at a rate of 10 °C/min and a dwell time of 1 h was applied at the peak temperature before cooling to room temperature. For each temperature, syntheses were carried out in two different gaseous conditions: in 100% Ar and in a mixture of Ar– H_2 (95–5%). In both cases, the gas flow rate was set to 1 mL/s. For target temperatures of 1500 and 1700 °C, yttria-stabilized zirconia crucibles were employed, and syntheses were carried out in pure Ar (5 mL/s). The temperature was raised at a rate of 5 °C/min, and a dwell time of 1 h was applied at the peak temperature before cooling to room temperature.

SEM Analysis. A field emission gun-scanning electron microscope Hitachi SU-70 was used to perform SEM analysis on samples *ex situ* annealed at 1500 and 1700 °C. Untreated grains as well as broken grains were deposited on carbon tape on SEM sample holders. The samples were not sputter-coated, and images were collected at a current voltage of 3 kV using SE (secondary electron) mode.

TEM Analysis. TEM imaging of *ex situ* annealed samples was performed by using a Jeol JEM-1400+ apparatus. The thermally processed powders were ground and dispersed in ethanol. Drops of the dispersion were deposited on a carbon film-coated copper TEM grid, and ethanol was allowed to evaporate under ambient conditions before analysis.

TEM-EDX. For elemental mapping of the oxide-embedded silicon particles, a ThermoFisher (FEI) Talos F200S G2 apparatus operating at 200 kV was used. Images were acquired using software VELOX (Version 2.13.1.1138-af4e0daa7d).

XRD Measurements. X-ray diffractograms from 8 to 80° 2θ were recorded on ground powders using a PANalytical X'Pert Pro apparatus (Cu radiation) equipped with an X'Celerator detector.

Solid-State NMR Spectroscopy. Solid-state NMR spectra were recorded using Bruker Avance III spectrometers equipped with either 7.05 or 11.7 T wide-bore superconducting magnets corresponding to the ^{29}Si Larmor frequency of 59.6 and 99.3 MHz, respectively. All data were acquired using 4 mm double-resonance Bruker MAS NMR probes, with a MAS rate of 10 kHz. Chemical shifts were referenced relative to silicon oil at –22 ppm, used as a secondary reference.

Direct excitation ^{29}Si MAS experiments were acquired by using a short pulse length of 3–4 μs corresponding to a selective $\pi/2$ pulse determined by silicon oil and a recycle interval of 60–400 s.

Although T_1 was very long for all ^{29}Si resonances, there was little difference in the relative relaxation rates and spectral intensities accurately reflected the relative site populations at 400 s.

For the experiments performed at different temperatures, although the cycle interval used (60 s) was not enough to take into account the different relative relaxation rates between silicon and silica, it allowed a comparison of the samples under equivalent conditions.

Raman Spectroscopy. A Horiba Xplora spectrometer equipped with a confocal microscope was used to collect Raman spectra. Selecting a probed area was done with a 10 \times objective lens and the focus of the laser beam on the sample with a 100 \times objective lens. The laser excitation wavelength was 633 nm, and a filter to reduce the laser power to 5% of the total power was used. To separate the scattered light into its components, a 600T grating was employed. Baseline subtraction was performed on each spectrum using a linear baseline. For each analyzed sample, Raman spectra were collected in seven different spots, assessing the reproducibility of the measurements.

ASSOCIATED CONTENT

Supporting Information

The Supporting Information is available free of charge at <https://pubs.acs.org/doi/10.1021/acs.chemmater.3c01448>.

Coalescence process (AVI)

Particle displacement in the matrix (MP4)
Coalescence followed by growth by displacement in the oxide (AVI)
HRTEM of crystalline Si domains formed at high temperature, ETEM images showing inhomogeneous nucleation, ETEM images of a probed region showing both particle coalescence and the particle growth mode by displacement in the matrix, *in situ* XRD diffractograms collected upon HSQ heating and cooling, weight loss after *ex situ* annealing under inert and reducing conditions, TEM images of the *ex situ* annealed sample under inert and reducing conditions, ^{29}Si MAS NMR spectra of an *ex situ* annealed sample at different temperatures, contributions of deconvoluted NMR signals, and additional Raman spectra of *ex situ* annealed samples (PDF)

AUTHOR INFORMATION

Corresponding Authors

Cynthia Cibaka-Ndaya – Univ. Bordeaux, CNRS, Bordeaux INP, ICMCB, UMR 5026, F-33600 Pessac, France;
Email: cynthia.cibaka@icmcb.cnrs.fr

Ioan-Lucian Roiban – Univ. Lyon, INSA Lyon, Université Claude Bernard Lyon 1, CNRS, MATEIS, UMR5510, 69621 Villeurbanne, France; orcid.org/0000-0003-1989-7367; Email: ioan-lucian.roiban@insa-lyon.fr

Glenna L. Drisko – Univ. Bordeaux, CNRS, Bordeaux INP, ICMCB, UMR 5026, F-33600 Pessac, France; orcid.org/0000-0001-6469-9736; Email: glenna.drisko@icmcb.cnrs.fr

Authors

Kevin O'Connor – Department of Chemistry, University of Alberta, Edmonton, Alberta T6G 2G2, Canada;
orcid.org/0000-0002-6400-6319

Emmanuel Opeyemi Idowu – Univ. Bordeaux, CNRS, Bordeaux INP, ICMCB, UMR 5026, F-33600 Pessac, France

Megan A. Parker – Univ. Bordeaux, CNRS, Bordeaux INP, ICMCB, UMR 5026, F-33600 Pessac, France

Eric Lebraud – Univ. Bordeaux, CNRS, Bordeaux INP, ICMCB, UMR 5026, F-33600 Pessac, France

Sabrina Lacomme – Univ. Bordeaux, CNRS, INSERM, Bordeaux Imaging Center, UAR 3420, F-33600 Pessac, France

David Montero – Sorbonne Université, CNRS, Fédération de Chimie et Matériaux de Paris-Centre, FR 2482, 75252 Paris, France

Paula Sanz Camacho – Univ. Bordeaux, CNRS, Bordeaux INP, ICMCB, UMR 5026, F-33600 Pessac, France

Jonathan G.-C. Veinot – Department of Chemistry, University of Alberta, Edmonton, Alberta T6G 2G2, Canada;
orcid.org/0000-0001-7511-510X

Complete contact information is available at:
<https://pubs.acs.org/10.1021/acs.chemmater.3c01448>

Notes

The authors declare no competing financial interest.

ACKNOWLEDGMENTS

This project is supported by funding from the European Research Council (ERC) under the European Union's Horizon 2020 research and innovation program (Scatter,

Grant agreement no. 948319). J.G.-C.V. and K.O. recognize funding from the Natural Science and Engineering Research Council (NSERC Discovery Grant program; RGPIN-2020-04045), Alberta Innovates, the ATUMS training program supported by NSERC CREATE (CREATE-463990-2015), and the University of Alberta Faculties of Science and Graduate Studies. The France, Canada Research Fund funded travel between the University of Alberta and the University of Bordeaux. The authors acknowledge the French national project METSA for providing them with access to the microscope platform of CLYM in Lyon. *In situ* XRD measurements were performed within the ICMCB X-ray facilities. Elemental analysis was performed at the Bordeaux Imaging Center, member of the FranceBioImaging national infrastructure (ANR-10-INBS-04). FEG-SEM observations were carried out at the Fédération de Chimie et Matériaux de Paris-Centre (FCMat FR2482), which was cofunded by Sorbonne Université, CNRS, and by the C'Nano projects of the Région Ile-de-France. TEM characterization of *ex situ* heated samples was performed using facilities of the platform PLACAMAT. Anthony Chiron assisted in the heat treatment of *ex situ* samples.

REFERENCES

- (1) De Marco, M. L.; Semlali, S.; Korgel, B. A.; Barois, P.; Drisko, G. L.; Aymonier, C. Silicon-Based Dielectric Metamaterials: Focus on the Current Synthetic Challenges. *Angew. Chem., Int. Ed.* **2018**, *57* (17), 4478–4498.
- (2) García-Etxarri, A.; Gómez-Medina, R.; Froufe-Pérez, L. S.; López, C.; Chantada, L.; Scheffold, F.; Aizpurua, J.; Nieto-Vesperinas, M.; Sáenz, J. J. Strong Magnetic Response of Submicron Silicon Particles in the Infrared. *Opt. Express* **2011**, *19* (6), 4815–4826.
- (3) Kustov, P.; Petrova, E.; Nazarov, M.; Gilmullin, A.; Sandomirskii, M.; Ponkratova, E.; Yaroshenko, V.; Ageev, E.; Zuev, D. Mie-Resonant Silicon Nanoparticles for Physically Unclonable Anti-Counterfeiting Labels. *ACS Appl. Nano Mater.* **2022**, *5* (8), 10548–10559.
- (4) Kruk, S.; Kivshar, Y. Functional Meta-Optics and Nanophotonics Governed by Mie Resonances. *ACS Photonics* **2017**, *4* (11), 2638–2649.
- (5) Zograf, G. P.; Ryabov, D.; Rutckaia, V.; Voroshilov, P.; Tonkaev, P.; Permyakov, D. V.; Kivshar, Y.; Makarov, S. V. Stimulated Raman Scattering from Mie-Resonant Subwavelength Nanoparticles. *Nano Lett.* **2020**, *20* (8), 5786–5791.
- (6) Dmitriev, P. A.; Baranov, D. G.; Milichko, V. A.; Makarov, S. V.; Mukhin, I. S.; Samusev, A. K.; Krasnok, A. E.; Belov, P. A.; Kivshar, Y. S. Resonant Raman Scattering from Silicon Nanoparticles Enhanced by Magnetic Response. *Nanoscale* **2016**, *8* (18), 9721–9726.
- (7) Eslamisaray, M. A.; Wray, P. R.; Lee, Y.; Nelson, G. M.; Ilic, O.; Atwater, H. A.; Kortshagen, U. R. A Single-Step Bottom-up Approach for Synthesis of Highly Uniform Mie-Resonant Crystalline Semiconductor Particles at Visible Wavelengths. *Nano Lett.* **2023**, *23* (5), 1930–1937.
- (8) Wray, P. R.; Eslamisaray, M. A.; Nelson, G. M.; Ilic, O.; Kortshagen, U. R.; Atwater, H. A. Broadband, Angle- and Polarization-Invariant Antireflective and Absorbing Films by a Scalable Synthesis of Monodisperse Silicon Nanoparticles. *ACS Appl. Mater. Interfaces* **2022**, *14* (20), 23624–23636.
- (9) Hessel, C. M.; Henderson, E. J.; Veinot, J. G. C. Hydrogen Silsesquioxane: A Molecular Precursor for Nanocrystalline Si–SiO₂ Composites and Freestanding Hydride-Surface-Terminated Silicon Nanoparticles. *Chem. Mater.* **2006**, *18* (26), 6139–6146.
- (10) Clark, R. J.; Aghajamali, M.; Gonzalez, C. M.; Hadidi, L.; Islam, M. A.; Javadi, M.; Mobarok, M. H.; Purkait, T. K.; Robidillo, C. J. T.; Sinelnikov, R.; Thiessen, A. N.; Washington, J.; Yu, H.; Veinot, J. G. C. From Hydrogen Silsesquioxane to Functionalized Silicon Nanocrystals. *Chem. Mater.* **2017**, *29* (1), 80–89.

- (11) Milliken, S.; Thiessen, A. N.; Cheong, I. T.; O'Connor, K. M.; Li, Z.; Hooper, R. W.; Robidillo, C. J. T.; Veinot, J. G. C. Turning the Dials[†]: Controlling Synthesis, Structure, Composition, and Surface Chemistry to Tailor Silicon Nanoparticle Properties. *Nanoscale* **2021**, *13* (39), 16379–16404.
- (12) Sugimoto, H.; Fujii, M. Colloidal Dispersion of Subquarter Micrometer Silicon Spheres for Low-Loss Antenna in Visible Regime. *Adv. Opt. Mater.* **2017**, *5* (17), No. 1700332.
- (13) Negoro, H.; Sugimoto, H.; Fujii, M. Helicity-Preserving Optical Metafluids. *Nano Lett.* **2023**, *23* (11), 5101–5107.
- (14) Sugimoto, H.; Okazaki, T.; Fujii, M. Mie Resonator Color Inks of Monodispersed and Perfectly Spherical Crystalline Silicon Nanoparticles. *Adv. Opt. Mater.* **2020**, *8* (12), No. 2000033.
- (15) Karsakova, M.; Shchedrina, N.; Karamyants, A.; Ponkratova, E.; Odintsova, G.; Zuev, D. Eco-Friendly Approach for Creation of Resonant Silicon Nanoparticle Colloids. *Langmuir* **2023**, *39* (1), 204–210.
- (16) Wang, J.; Wang, X. F.; Li, Q.; Hryciw, A.; Meldrum, A. The Microstructure of SiO Thin Films: From Nanoclusters to Nanocrystals. *Philos. Mag.* **2007**, *87* (1), 11–27.
- (17) Garrido Fernandez, B.; López, M.; García, C.; Pérez-Rodríguez, A.; Morante, J. R.; Bonafos, C.; Carrada, M.; Claverie, A. Influence of Average Size and Interface Passivation on the Spectral Emission of Si Nanocrystals Embedded in SiO₂. *J. Appl. Phys.* **2002**, *91* (2), 798–807.
- (18) Choe, H.-W.; Woo, H.-J.; Kim, J.-K.; Kim, G.-D.; Hong, W.-H.; Ji, Y.-Y. Encapsulated Silicon Nanocrystals Formed in Silica by Ion Beam Synthesis. *Bull. Korean Chem. Soc.* **2004**, *25* (4), 525–528.
- (19) Yang, Z.; Dobbie, A. R.; Cui, K.; Veinot, J. G. C. A Convenient Method for Preparing Alkyl-Functionalized Silicon Nanocubes. *J. Am. Chem. Soc.* **2012**, *134* (34), 13958–13961.
- (20) Bonafos, C.; Garrido, B.; Lopez, M.; Perez-Rodriguez, A.; Morante, J. R.; Kihn, Y.; Ben Assayag, G.; Claverie, A. Ostwald Ripening of Ge Precipitates Elaborated by Ion Implantation in SiO₂. *Mater. Sci. Eng., B* **2000**, *69–70*, 380–385.
- (21) Yu, D.; Lee, S.; Hwang, G. S. On the Origin of Si Nanocrystal Formation in a Si Suboxide Matrix. *J. Appl. Phys.* **2007**, *102* (8), No. 084309.
- (22) Hessel, C. M.; Henderson, E. J.; Veinot, J. G. C. An Investigation of the Formation and Growth of Oxide-Embedded Silicon Nanocrystals in Hydrogen Silsesquioxane-Derived Nanocomposites. *J. Phys. Chem. C* **2007**, *111* (19), 6956–6961.
- (23) Sato, K.; Izumi, T.; Iwase, M.; Show, Y.; Morisaki, H.; Yaguchi, T.; Kamino, T. Nucleation and Growth of Nanocrystalline Silicon Studied by TEM, XPS and ESR. *Appl. Surf. Sci.* **2003**, *216* (1), 376–381.
- (24) Xin, Y.; Wakimoto, R.; Saitow, K. Synthesis of Size-Controlled Luminescent Si Nanocrystals from (HSiO_{1.5})_n Polymers. *Chem. Lett.* **2017**, *46* (5), 699–702.
- (25) Belot, V.; Corriu, R.; Leclercq, D.; Mutin, P. H.; Vioux, A. Thermal Reactivity of Hydrogenosilsesquioxane Gels. *Chem. Mater.* **1991**, *3* (1), 127–131.
- (26) Hartman, J. S.; Richardson, M. F.; Sherriff, B. L.; Winsborrow, B. G. Magic Angle Spinning NMR Studies of Silicon Carbide: Polytypes, Impurities, and Highly Inefficient Spin-Lattice Relaxation. *J. Am. Chem. Soc.* **1987**, *109* (20), 6059–6067.
- (27) Lee, D.; Kaushik, M.; Coustel, R.; Chenavier, Y.; Chanal, M.; Bardet, M.; Dubois, L.; Okuno, H.; Rochat, N.; Duclairoir, F.; Mouesca, J.; De Paëpe, G. Solid-State NMR and DFT Combined for the Surface Study of Functionalized Silicon Nanoparticles. *Chem. - Eur. J.* **2015**, *21* (45), 16047–16058.
- (28) Pietraß, T.; Bifone, A.; Roth, R. D.; Koch, V.-P.; Alivisatos, A. P.; Pines, A. ²⁹Si High Resolution Solid State Nuclear Magnetic Resonance Spectroscopy of Porous Silicon. *J. Non-Cryst. Solids* **1996**, *202* (1), 68–76.
- (29) Shao, W.; Shinar, J.; Gerstein, B. C.; Li, F.; Lannin, J. S. Magic-Angle Spinning ²⁹Si NMR Study of Short-Range Order in a-Si. *Phys. Rev. B* **1990**, *41* (13), 9491–9494.
- (30) Faulkner, R. A.; DiVerdi, J. A.; Yang, Y.; Kobayashi, T.; Maciel, G. E. The Surface of Nanoparticle Silicon as Studied by Solid-State NMR. *Materials* **2013**, *6* (1), 18–46.
- (31) Mayeri, D.; Phillips, B. L.; Augustine, M. P.; Kauzlarich, S. M. NMR Study of the Synthesis of Alkyl-Terminated Silicon Nanoparticles from the Reaction of SiCl₄ with the Zintl Salt, NaSi. *Chem. Mater.* **2001**, *13* (3), 765–770.
- (32) Caylor, R. A. *Towards the Characterization of Silicon Surfaces: Solid State Nuclear Magnetic Resonance*; Colorado State University, Fort Collins, CO, 2011.
- (33) Thiessen, A. N.; Ha, M.; Hooper, R. W.; Yu, H.; Oliynyk, A. O.; Veinot, J. G. C.; Michaelis, V. K. Silicon Nanoparticles: Are They Crystalline from the Core to the Surface. *Chem. Mater.* **2019**, *31* (3), 678–688.
- (34) Richter, H.; Wang, Z. P.; Ley, L. The One Phonon Raman Spectrum in Microcrystalline Silicon. *Solid State Commun.* **1981**, *39* (5), 625–629.
- (35) Harris, J. T.; Hueso, J. L.; Korgel, B. A. Hydrogenated Amorphous Silicon (a-Si:H) Colloids. *Chem. Mater.* **2010**, *22* (23), 6378–6383.
- (36) De Marco, M. L.; Jiang, T.; Fang, J.; Lacomme, S.; Zheng, Y.; Baron, A.; Korgel, B. A.; Barois, P.; Drisko, G. L.; Aymonier, C. Broadband Forward Light Scattering by Architectural Design of Core-Shell Silicon Particles. *Adv. Funct. Mater.* **2021**, *31* (26), No. 2100915.
- (37) Tsu, D. V.; Chao, B. S.; Jones, S. J. Intermediate Order in Tetrahedrally Coordinated Silicon: Evidence for Chainlike Objects. *Sol. Energy Mater. Sol. Cells* **2003**, *78* (1), 115–141.
- (38) Hong, W.-E.; Ro, J.-S. Kinetics of Solid Phase Crystallization of Amorphous Silicon Analyzed by Raman Spectroscopy. *J. Appl. Phys.* **2013**, *114* (7), No. 073511.
- (39) Morhange, J. F.; Kanellis, G.; Balkanski, M. Raman Study of Laser Annealed Silicon. *Solid State Commun.* **1979**, *31* (11), 805–808.
- (40) Tsu, R.; Izu, M.; Ovshinsky, S. R.; Pollak, F. H. Electroreflectance and Raman Scattering Investigation of Glow-Discharge Amorphous Si:F:H. *Solid State Commun.* **1980**, *36* (9), 817–822.
- (41) Anastassakis, E.; Pinczuk, A.; Burstein, E.; Pollak, F. H.; Cardona, M. Effect of Static Uniaxial Stress on the Raman Spectrum of Silicon. *Solid State Commun.* **1993**, *88* (11), 1053–1058.